

# Simultaneous measurement of bubble size, velocity and void fraction in two-phase bubbly flows with time-resolved X-ray imaging

Sung Yong Jung,<sup>a,b</sup> Han Wook Park<sup>a,b</sup> and Sang Joon Lee<sup>a,b\*</sup>

<sup>a</sup>Department of Mechanical Engineering, Pohang University of Science and Technology (POSTECH), San 31, Hyojadong, Pohang 790-784, Republic of Korea, and <sup>b</sup>Center for Biofluid and Biomimic Research, Pohang University of Science and Technology (POSTECH), San 31, Hyojadong, Pohang 790-784, Republic of Korea. \*E-mail: sjlee@postech.ac.kr

Key parameters of two-phase flows, such as void fraction and microscale bubble size, shape and velocity, were simultaneously measured using time-resolved X-ray imaging. X-ray phase-contrast imaging was employed to obtain those parameters on microbubbles. The void fraction was estimated from X-ray absorption. The radii of the measured microbubbles were mostly smaller than 20  $\mu\text{m}$ , and the maximum velocity was 39.442  $\text{mm s}^{-1}$ , much higher than that in previous studies. The spatial variations of the void fraction were consecutively obtained with a small time interval. This technique would be useful in the experimental analysis of bubbly flows in which microbubbles move at high speed.

**Keywords:** X-ray imaging; bubbly flow; void fraction; bubble size; bubble velocity.

## 1. Introduction

Gas–liquid flows in which gas is dispersed in liquid occur in various fields, from natural to industrial processes. Bubbly flows are a common subset of gas–liquid flows encountered in various industrial processes, such as oil transportation, nuclear cooling, mineral separation, metal purification, solid fuel liquefaction, and gas–liquid chemical reactors (Finch & Dobby, 1991; Kantarci *et al.*, 2005; Poullikkas, 2003; Saxena *et al.*, 1988; Stevenson *et al.*, 2008; Tayler *et al.*, 2012). Bubbly flows are also used in medical imaging for the human body with microbubbles as the contrast agent (Wei *et al.*, 1997; Veltman *et al.*, 2002). Volumetric void fraction, the volumetric ratio of the gas phase in a gas–liquid two-phase flow, is one of the most important physical parameters in the analysis of two-phase flows. The size and velocity of each bubble govern the flow characteristics of the two-phase flow. Therefore, accurate measurements of the shape, size and velocity of bubbles and void fraction are essential for a fundamental understanding of bubbly flows.

Many experimental techniques, such as optical imaging (Hassan *et al.*, 2001; Majumder *et al.*, 2006), acoustic imaging (Manasseh *et al.*, 2001), electric sensing (Saxena *et al.*, 1988; Uesawa *et al.*, 2012), neutron radiography (Asano *et al.*, 2004; Saito *et al.*, 2005) and magnetic resonance imaging (MRI) (Tayler *et al.*, 2012; Daidzic *et al.*, 2005), have been used in the experimental analysis of bubbly flows. However, these conventional methods have various inherent restrictions. Electric sensing has good temporal resolution but poor spatial

resolution ( $\sim 1$  mm). An invasive probe also induces systematic errors, because it distorts the surrounding flow. Optical imaging techniques have been employed with transparent conduits and are limited to relatively low voidage flows. Acoustic imaging also fails at high voidages because of strong pressure fluctuations caused by bubble interactions. Neutron radiography and MRI can measure three-dimensional flow structures. However, these techniques have low spatial and temporal resolutions. Therefore, these methods have difficulty identifying individual microbubbles or investigating highly fluctuating bubbly flows.

X-ray imaging techniques using a fan-beam-type medical X-ray tube (Aeschlimann *et al.*, 2011; Baker & Bonazza, 1998; Bauer *et al.*, 2012; Chaouki *et al.*, 1997; Fischer *et al.*, 2008; Heindel, 2011; Kendoush & Sarkis, 2002; Seeger *et al.*, 2002, 2004) and synchrotron X-ray beams (Jung *et al.*, 2012; Lee & Kim, 2003, 2005; Lee & Socha, 2009; Lin *et al.*, 2011; Vabre *et al.*, 2009) have been used for two-phase flow measurements. In X-ray imaging experiments using a medical X-ray tube, the spatial and temporal resolution are relatively poor and only the absorption-contrast imaging method is available. Even though X-ray attenuation is effective in the estimation of the void fraction, the absorption contrast imaging is relatively inadequate for accurately detecting the interface between two-phase flows, compared with the phase-contrast imaging method utilizing synchrotron X-ray beams.

The synchrotron X-ray imaging technique provides high spatial and temporal resolutions for investigating two-phase flow phenomena. It can utilize both the absorption- and phase-

contrast imaging mechanisms at the same time. In previous studies using synchrotron X-ray beams, the motions of bubbles or particles have been analyzed by using only one of the absorption- or phase-contrast imaging methods. The void fraction of a gas–liquid mixture can be clearly detected based on the different X-ray absorption rates of liquid and gas. However, there is no previous study that uses the advantages of X-ray attenuations in the estimation of the void fraction of two-phase flows using synchrotron X-rays. The absorption- and phase-contrast imaging methods are effective for estimating the void fraction and detecting interfaces of bubbly two-phase flows, respectively. However, all previous studies used only one of the X-ray imaging methods in two-phase flow experiments.

The main purpose of this study is to demonstrate the effectiveness of the adaptively combined synchrotron X-ray imaging technique in simultaneous measurements of the void fraction and flow characteristics of bubbly two-phase flows.

In this study, the key parameters of two-phase flows, such as void fraction and the shape, size and velocity of microbubbles, were simultaneously measured by time-resolved X-ray imaging technique. Digital image processing methods were used to obtain the shape, size and velocity of microbubbles from phase-contrast X-ray images. The void fraction was estimated based on the spatial distribution of different X-ray absorption rates. This experimental method was validated with both simulated and experimentally acquired X-ray images. The results confirm that various features of two-phase flows can be simultaneously measured with high spatial and temporal resolutions.

## 2. Measurement of the shape, size and velocity of microbubbles

A coherent X-ray beam induces Fresnel edge diffraction patterns in radiological images. In this study, synchrotron X-ray imaging was employed to determine the shape and size of microbubbles moving in a fluid by analyzing their Fresnel

diffraction patterns induced by the different refractive indices of gas and liquid at the interface between the liquid and gas. The resulting diffraction patterns in the X-ray images clearly delineated the exact shape of each bubble. The interface between the liquid and gas phases was detected through a Canny edge detection algorithm (Canny, 1986). After the edge detection, the shape and size of each bubble were determined with a generalized Hough transform, which has commonly been used as a feature extraction technique (Ballard, 1981). Instantaneous velocity fields of the microbubbles were measured by applying two-frame particle tracking velocimetry (PTV) (Baek & Lee, 1996) to the center position of microbubbles obtained from the Hough transform. Two-frame PTV tracks the displacement vector of each matched particle pair in consecutive image frames.

The usefulness of the developed method was tested through a simulated X-ray image with both absorption- and phase-contrast effects. The Kirchoff formula was used to calculate the intensity distribution of the simulated image (Cowley, 1975; Stevenson *et al.*, 2003). Intensity distribution can be described by the following equations,

$$I(x, y) = |U(x_0, y_0)|^2, \quad x_0 = x(Z_0/Z_t), \quad y_0 = y(Z_0/Z_t), \quad (1)$$

$$U(x_0, y_0) = \iint U(x_1, y_1) \frac{1}{(i\lambda Z)^{1/2}} \times \exp\left\{\frac{i\pi}{\lambda Z}[(x_0 - x_1)^2 + (y_0 - y_1)^2]\right\} dx_1 dy_1, \quad (2)$$

where  $Z_0$  is the distance between the X-ray source and the test object,  $Z_1$  is the distance from the object to the detector,  $Z_t = Z_0 + Z_1$ ,  $Z = Z_0 Z_1 / Z_t$  and  $U(x_1, y_1)$  represents an object.

A time-resolved X-ray imaging system (Fig. 1) was used to validate the method experimentally. The experiment was conducted at the 6D beamline of the Pohang Light Source (PLS-II) in Pohang, Republic of Korea. The maximum beam current and storage energy of the PLS-II were 400 mA and

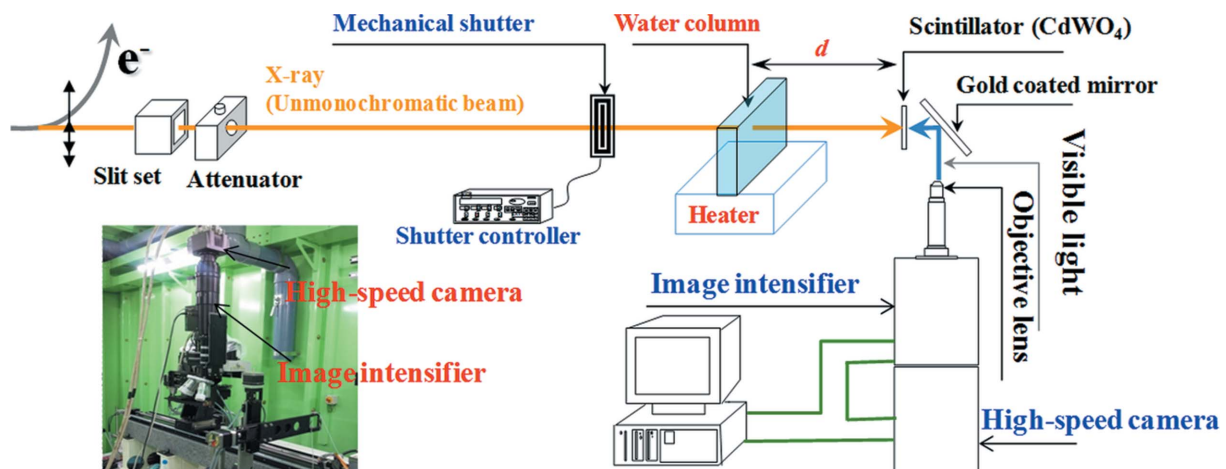


**Figure 1**  
Schematic diagram of the time-resolved X-ray imaging system.

3 GeV, respectively. A 125 mA beam current was used in this study. An image intensifier (Lambert Instrument, HiCATT) was positioned in front of a high-speed camera (Photron, FASTCAM Ultima APX) at a full resolution of  $1024 \times 1024$  pixels. The field of view with a  $10\times$  objective lens in front of the camera had physical dimensions of  $1.6 \text{ mm} \times 1.6 \text{ mm}$ . The X-ray beamline and imaging devices are described in detail by Jung *et al.* (2013).

The actual situation of the synchrotron X-ray beam was used in the simulation study. A spherical air bubble suspended in water was numerically simulated. Figs. 2(a-I) to 2(a-V) show the simulated X-ray images as a function of  $Z_1$ . At  $Z_1 = 0.1 \text{ cm}$ , an edge diffraction pattern did not appear because the intensity distributions were dominated by absorption contrast

with little contribution from phase contrast. Increasing  $Z_1$  increased the contribution from phase contrast but weakened that from absorption contrast. At  $Z_1 > 30 \text{ cm}$ , the diffraction fringe pattern became obvious at the edge. Fig. 2(a-VI) shows the binary image obtained by applying the developed algorithm at  $Z_1 = 50 \text{ cm}$ , which is a commonly used experimental condition. The edge image was successfully obtained, and the center position and size of the bubble were accurately evaluated by the developed method.

Bubbly flows were generated by heating water in a 5 mm-thick rectangular channel. The internal dimension of the rectangular channel was  $30 \text{ mm} \times 70 \text{ mm}$ , and X-ray images were captured in the center area of the rectangular channel. The water column was placed approximately 30 m downstream from the X-ray source, and the image detector was located 50 cm downstream from the sample. X-ray images of bubbly flows in the water column were consecutively recorded at  $1000 \text{ frames s}^{-1}$ . The field of view in Fig. 2(b) is  $1.0 \text{ mm} \times 1.0 \text{ mm}$ . Raw X-ray images have low contrast with granular patterns because of short exposure time and the granular-shaped structural feature of the image intensifier. Therefore, digital image processing techniques were adopted to improve image quality before applying the edge detection algorithm. Flat-field correction, median filter, spatial-frequency filter and a contrast-limited adaptive histogram equalization algorithm were applied in consecutive order. We investigated the effectiveness of such techniques in our previous study (Jung *et al.*, 2013).

Fig. 2(b-I) shows a typical instantaneous X-ray raw image of microbubbles in de-ionized water. The size and velocity distribution extracted from the X-ray image are shown in Figs. 2(b-II) and 2(b-III), respectively. The Hough transform used to determine bubble shape effectively extracted both elliptical and circular features. In Figs. 2(b-I) and 2(b-II) the bubble diameter in the horizontal direction is similar to that in the vertical direction, indicating that the measured microbubbles were almost perfect spheres. The probability density functions of the measured bubble radii and average velocities are shown in Fig. 2(c). The number of measured bubbles in 2048 consecutive images was about 22835. The error bars in Fig. 2(c) represent the standard deviation of the bubble velocities. Stokes' law states that the theoretical terminal velocity of rising microbubbles in a standstill liquid is proportional to the square of the bubble size (Lee & Kim, 2005). However, the rising velocities measured in this study are almost independent of bubble size. The average and maximum velocities are  $11.596$  and  $39.442 \text{ mm s}^{-1}$ , respectively. The theoretical terminal velocity calculated using Stokes' law is  $0.777 \text{ mm s}^{-1}$  for a vessel of diameter  $20 \mu\text{m}$ . This result indicates that water flow has more significant influence on the rising motion of bubbles, compared with buoyancy. This maximum velocity was significantly higher than that in a previous study ( $2.5 \text{ mm s}^{-1}$ ; Lee & Kim, 2005). The radius of most bubbles was smaller than  $20 \mu\text{m}$ . Microbubbles in this diameter range are suitable contrast agents in biomedical diagnosis to obtain biological flow information. Therefore, this method using microbubbles as tracer particles

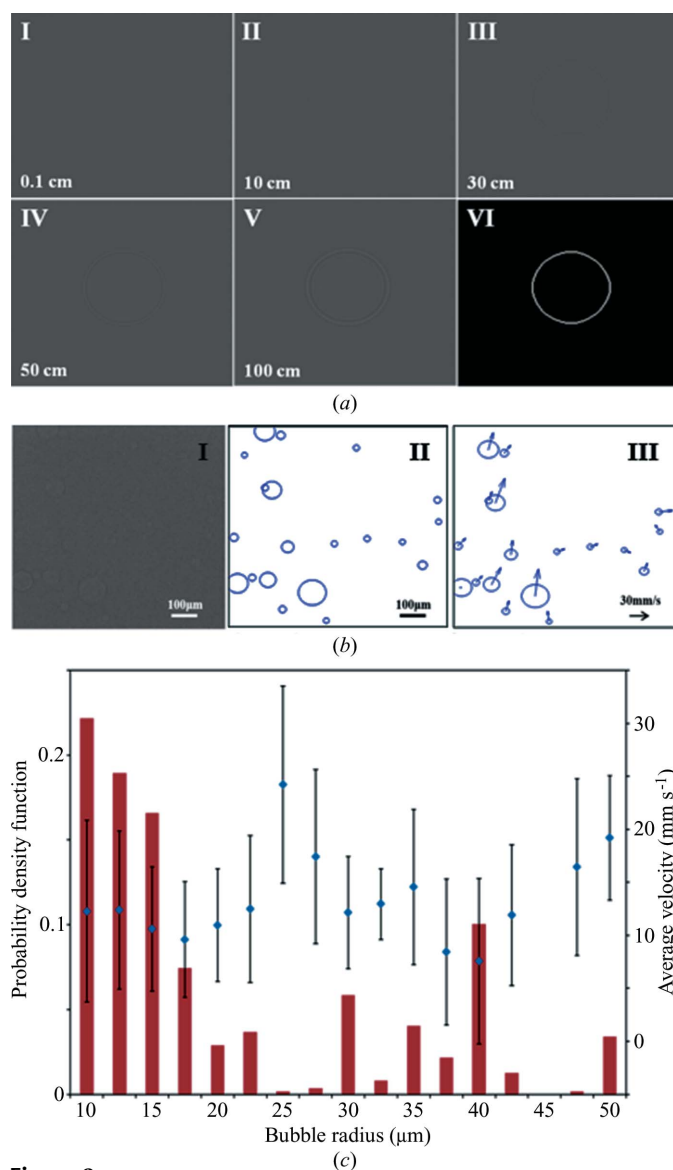


**Figure 2** (a) Simulated X-ray images at various distances  $Z_1$  from the test object to detector (I–V). The binary image was obtained by Canny edge detection and the generalized Hough transform at  $Z_1 = 50 \text{ cm}$  (VI). (b) Typical instantaneous X-ray raw image (I). Spatial distributions of size (II) and velocity (III) of rising microbubbles. (c) Probability density functions and average velocities of microbubbles according to bubble radius.

is suitable for measuring high-speed blood flows in actual physiological conditions.

### 3. Measurement of the void fraction

The X-ray energy transmitted through an absorbent material is attenuated according to the Beer–Lambert law (Cullity, 1978),

$$I = I_0 \exp(-\mu x), \quad (3)$$

where  $\mu$  is the linear absorption coefficient of the material and  $I_0$  and  $I$  are the incident and transmitted intensities of the X-ray beam, respectively.

The void fraction ( $\alpha$ ) is the ratio of vapor volume to the total measurement volume. For a given X-ray beam, the void ratio can be expressed as

$$\alpha = x_g / (x_g + x_l), \quad (4)$$

where  $x_l$  and  $x_g$  are the integrated thicknesses of the liquid and gas phases, respectively, along the X-ray beam.

Based on equations (3) and (4) the void fraction was calculated as

$$\alpha = (\ln I_t - \ln I_l) / (\ln I_g - \ln I_l), \quad (5)$$

where  $I_g$  and  $I_l$  are the intensities measured at the test section filled with gas ( $\alpha = 1$ ) and liquid ( $\alpha = 0$ ), respectively, and  $I_t$  is the intensity of the gas–liquid mixture at time  $t$ .  $I_g$  and  $I_l$  were obtained by averaging 100 images.

Fresnel diffraction at the interface between the gas and liquid phases brings about intensity fluctuations in the normal direction of the interface. These fluctuations cause an error in the estimation of the void fraction based on intensities measured according to equation (5). The intensity fluctuations caused by diffraction are observed in a specific range (seven pixels in this experiment) from the interface. To reduce the diffraction effect on the calculation of the void fraction, the intensities in this range were interpolated with a linear curve fitting along the normal direction by using the information on the interface shape and position extracted by the Canny edge detection algorithm and generalized Hough transform. Intensity also fluctuated over the whole region because of image noise but was eventually stabilized by a median filter.

To verify the reliability of the void fraction measurements, errors in the measurements were analyzed by comparing the experimentally measured void fraction with the theoretical value,

$$\text{Error} = \frac{1}{N \times (x_{\text{pixels}} \times y_{\text{pixels}})} \sum_{n=1}^N \sum_{i=1}^{x_{\text{pixels}}} \sum_{j=1}^{y_{\text{pixels}}} |\alpha_{Tij} - \alpha_{Eij}|_n, \quad (6)$$

where  $x_{\text{pixels}}$  and  $y_{\text{pixels}}$  are the number of pixels in the row and column, respectively (both 1024), and  $N$  is the number of statistically averaged images. The error analysis tested 100 images filled with air. The theoretical void fraction  $\alpha_{Tij}$  was 1 in this case. The error was found to be 0.0213, which corresponds to a 2.13% error. The standard deviation was about 0.0144. To

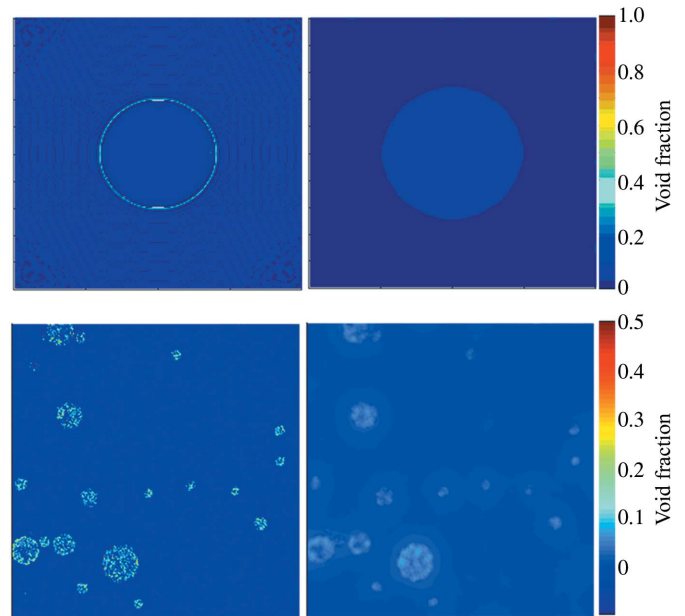


**Figure 3** Void fraction distributions before (left) and after (right) digital image processing techniques were used to reduce intensity fluctuations. The upper and lower images show the simulation and experimental results, respectively.

evaluate the aforementioned processing efficiency of reducing intensity fluctuations in void fraction measurements, the error was also analyzed using the X-ray images with the test section filled with a gas–liquid mixture. As shown in Fig. 2(b), the size and position of the microbubbles were successfully obtained. The microbubbles were almost perfect spheres. Therefore, the thickness of the air column along the X-ray beam [ $x_g$  in (4)] can be evaluated. The test channel has uniform thickness. Assuming that water completely filled the test section while excluding the gas volume occupied by the microbubbles, the theoretical  $\alpha_{Tij}$  can be estimated based on the measured information on the microbubbles. Over the entire field of view, the errors without and with digital image processing techniques were 0.0789 and 0.0041, respectively. The local error inside the microbubbles was also analyzed, because large errors occurred inside the microbubbles. The local errors without and with the image-processing techniques were 0.2049 and 0.0132, respectively. These results show that the digital image processing techniques effectively reduce the effect of intensity fluctuations, especially inside microbubbles. The effectiveness of the processing is graphically shown in Fig. 3.

To examine the feasibility of measuring the void fraction of highly fluctuating flows, the void fraction of the film boiling phenomena was measured experimentally. Fig. 4(a) shows a typical temporal variation of the void fraction and a snapshot of the two-phase flow in a film boiling state (a movie clip is available in the supporting information<sup>1</sup>). The void fraction was statistically averaged over the whole field of view. Both the size and the number of generated bubbles are increased with increasing heating temperature. In the narrow water

<sup>1</sup> Supporting information for this paper is available from the IUCr electronic archives (Reference: PP5041).

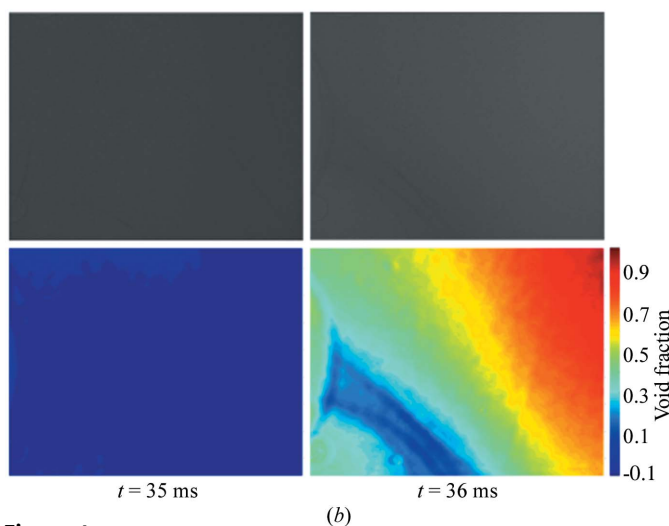
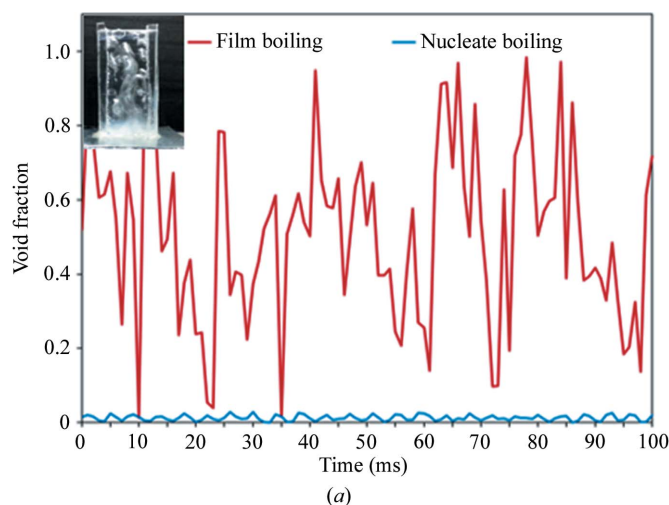


**Figure 4** (a) Temporal variation of void fraction and a typical snapshot of two-phase flow at film boiling state (a movie clip is available in the supporting information). (b) Consecutive X-ray images (upper images) and spatial distributions of void fraction (lower images) at  $t = 35$  and  $36$  ms.

channel of this experiment, large bubbles and a fluctuating air column are formed. The interface of two-phase flows is dynamically changed under a film boiling state. In a nucleate boiling state, the different void fraction is caused by the changes in the size and number of bubbles. Therefore, the variation in the void fraction in a nucleate boiling state is smaller compared with the void fraction fluctuations in a film boiling state. Two consecutive X-ray images and the void fraction distributions at  $t = 35$  and  $36$  ms are shown in Fig. 4(b). The void fraction suddenly changed in a short interval of 1 ms. In addition to the temporal variation, the spatial distributions of the void fraction and interface of the two-phase flows were observed at the instant  $t = 36$  ms.

#### 4. Conclusion

Several important physical properties of two-phase flows, such as the shape, size and velocity of microbubbles and the void fraction, were simultaneously measured with high spatial and

temporal resolutions. X-ray phase-contrast imaging, particularly Fresnel diffraction, was employed to obtain microbubble information. Canny edge detection and generalized Hough transform were used to measure the shape, size and position of the microbubbles, and the two-frame PTV algorithm was used to measure the displacement of the microbubbles. The void fraction was estimated from X-ray absorption according to the Beer–Lambert law and the definition of the void fraction. The problems encountered in void fraction measurement were overcome by adopting digital image processing techniques. The void fraction of highly fluctuating flows was accurately determined by the present method with high temporal and spatial resolutions. This technique contributes to the design and performance evaluation of two-phase flows in practical applications in which microscale bubbles move quickly, such as medical imaging, water purification and gas–liquid reactors.

This work was supported by a National Research Foundation of Korea (NRF) grant funded by the Korea government (MSIP) (No. 2008-0061991). The authors thank the people who helped in their X-ray imaging experiments at the 6D beamlines of the Pohang Accelerator Laboratory (Pohang, Korea).

#### References

Aeschlimann, V., Barre, S. & Legoupil, S. (2011). *Phys. Fluids*, **23**, 055101.  
 Asano, H., Takenaka, N. & Fujii, T. (2004). *Exp. Therm. Fluid Sci.* **28**, 223–230.  
 Baek, S. J. & Lee, S. J. (1996). *Exp. Fluids*, **22**, 23–32.  
 Baker, M. C. & Bonazza, R. (1998). *Exp. Fluids*, **22**, 61–68.  
 Ballard, D. H. (1981). *Pattern Recognit.* **13**, 111–122.  
 Bauer, D., Chaves, H. & Arcoumanis, C. (2012). *Meas. Sci. Technol.* **23**, 055302.  
 Canny, J. (1986). *IEEE Trans. Pattern Anal. Mach. Intell.* **8**, 679–698.  
 Chaouki, J., Larachi, F. & Duduković, M. P. (1997). *Ind. Eng. Chem. Res.* **36**, 4476–4503.  
 Cowley, J. M. (1975). *Diffraction Physics*. Amsterdam: North-Holland.  
 Cullity, B. D. (1978). *Elements of X-ray Diffraction*. New York: Addison-Wesley.  
 Daidzic, N., Schmidt, E., Hasan, M. & Altobelli, S. (2005). *Nucl. Eng. Des.* **235**, 1163–1178.  
 Finch, J. A. & Dobby, G. S. (1991). *Int. J. Min. Proc.* **33**, 343–354.  
 Fischer, F., Hoppe, D., Schleicher, E., Mattausch, G., Flaske, H., Bartel, R. & Hampel, U. (2008). *Meas. Sci. Technol.* **19**, 094002.  
 Hassan, Y. A., Ortiz-Villafuerte, J. & Schmidl, W. D. (2001). *Int. J. Multiphase Flow*, **27**, 817–842.  
 Heindel, T. J. (2011). *J. Fluids Eng.* **133**, 074001.  
 Jung, S. Y., Ahn, S., Nam, K. H., Lee, J. P. & Lee, S. J. (2012). *Int. J. Cardiovasc. Imaging*, **28**, 1853–1858.  
 Jung, S. Y., Park, H. W., Kim, B. H. & Lee, S. J. (2013). *J. Synchrotron Rad.* **20**, 498–503.  
 Kantarci, N., Borak, F. & Ulgen, K. O. (2005). *Process Biochem.* **40**, 2263–2283.  
 Kendoush, A. A. & Sarkis, Z. A. (2002). *Exp. Therm. Fluid Sci.* **25**, 615–621.  
 Lee, S. & Kim, G. (2003). *J. Appl. Phys.* **94**, 3620.  
 Lee, S. J. & Kim, S. (2005). *Exp. Fluids*, **39**, 492–497.  
 Lee, W. K. & Socha, J. J. (2009). *BMC Physiol.* **9**, 2.  
 Lin, K. C., Rajnicek, C., McCall, J., Carter, C. & Fezzaa, K. (2011). *Nucl. Instrum. Methods Phys. Res. A*, **649**, 194–196.

- Majumder, S. K., Kundu, G. & Mukherjee, D. (2006). *Chem. Eng. J.* **112**, 1–10.
- Manasseh, R., LaFontaine, R. F., Davy, J., Shepherd, I. & Zhu, Y. G. (2001). *Exp. Fluids*, **30**, 672–682.
- Poullikkas, A. (2003). *Prog. Nucl. Energ.* **42**, 3–10.
- Saito, Y., Mishima, K., Matsubayashi, M., Lim, I. C., Cha, J. E. & Sim, C. H. (2005). *Nucl. Instrum. Methods Phys. Res. A*, **542**, 309–315.
- Saxena, S. C., Patel, D., Smith, D. N. & Ruether, J. A. (1988). *Chem. Eng. Commun.* **63**, 87–127.
- Seeger, A., Affeld, K., Goubergrits, L., Kertzsch, U., Wellnhofer, E. & Delfos, R. (2002). *Ann. NY Acad. Sci.* **972**, 247–253.
- Seeger, A., Kertzsch, D., Affeld, K., Goubergrits, L. & Wellnhofer, E. (2004). *Heat Mass Transfer*, **40**, 129–138.
- Stevenson, A. W., Gureyev, T. E., Paganin, D., Wilkins, S. W., Weitkamp, T., Snigirev, A., Rau, C., Snigireva, I., Youn, H. S., Dolbnya, I. P., Yun, W., Lai, B., Garrett, R. F., Cookson, D. J., Hyodo, K. & Ando, M. (2003). *Nucl. Instrum. Methods Phys. Res. B*, **199**, 427–435.
- Stevenson, P., Fennell, P. S. & Galvin, K. P. (2008). *Can. J. Chem. Eng.* **86**, 635–642.
- Taylor, A. B., Holland, D. J., Sederman, A. J. & Gladden, L. F. (2012). *Chem. Eng. Sci.* **71**, 468–483.
- Uesawa, S., Kaneko, A. & Abe, Y. (2012). *Flow Meas. Instrum.* **24**, 50–62.
- Vabre, A., Gmar, M., Lazaro, D., Legoupil, S., Coutier, O., Dazin, A., Lee, W. K. & Fezzaa, K. (2009). *Nucl. Instrum. Methods Phys. Res. A*, **607**, 215–217.
- Veltman, J., Goossen, T., Laguna, P., Wijkstra, H. & de la Rosette, J. (2002). *Eur. Urol. Suppl.* **1**, 8–14.
- Wei, K., Skyba, D. M., Firschke, C., Jayaweera, A. R., Lindner, J. R. & Kaul, S. (1997). *J. Am. Collect. Cardiol.* **29**, 1081–1088.